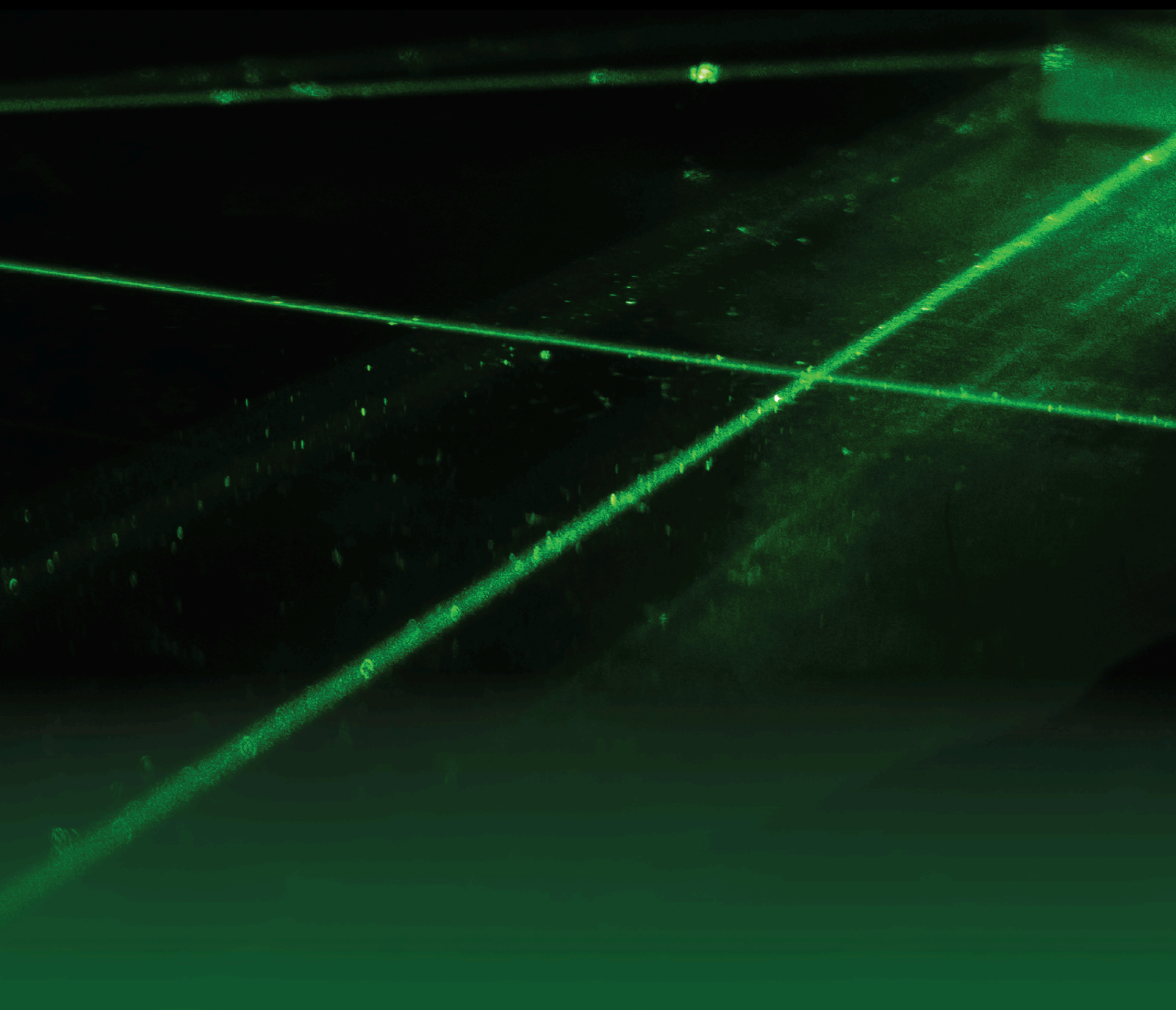# Conference Issue: Laser Matter Interaction at ECLIM 2022

Lead Guest Editor: Riccardo De Angelis
Guest Editors: J. Manuel Perlado, Shalom Eliezer, and Fabrizio Consoli

Conference Issue: Laser Matter Interaction at ECLIM 2022

Conference Issue: Laser Matter Interaction at ECLIM 2022

Lead Guest Editor: Riccardo De Angelis
Guest Editors: J. Manuel Perlado, Shalom Eliezer, and Fabrizio Consoli

Chief Editor

Katarzyna Batani, Poland

Chief Editor Emeritus

Dieter H. H. Hoffmann, Germany

Academic Editors

Dimitri Batani, France
Yuji Fukuda, Japan
Ahmed Hassanein, USA
Daniele Margarone, United Kingdom
Devki Nandan Gupta, India
Vincenzo Palleschi, Italy
Jose Manuel Perlado, Spain
Sergey Pikuz, Russia
Bhuvanesh Ramakrishna, India
Tao Shao, China
Xinxin Wang, China
Mingsheng Wei, USA
Yongtao Zhao, China
Zongqing Zhao, China

Advisory Board Member(s)

Contents

Research Article

Numerical Study of Carbon Nanofoam Targets for Laser-Driven Inertial Fusion Experiments

A. Maffini ⬤,[1] M. Cipriani ⬤,[2] D. Orecchia,[1] V. Ciardiello,[1,2] A. Formenti,[1] F. Consoli ⬤,[2] and M. Passoni[1]

[1]*Energy Department, Politecnico di Milano, Piazza Leonardo da Vinci 33, Milan 20133, Italy*
[2]*ENEA, Fusion and Technologies for Nuclear Safety Department, C.R. Frascati, Frascati 00044, Italy*

Correspondence should be addressed to A. Maffini; alessandro.maffini@polimi.it and M. Cipriani; mattia.cipriani@enea.it

Porous materials have peculiar characteristics that are relevant for inertial confinement fusion (ICF). Among them, chemically produced foams are proved to be able to smooth the laser inhomogeneities and to increase the coupling of the laser with the target. Foams realized with other elements and techniques may prove useful as well for ICF applications. In this work, we explore the potential of a novel class of porous materials for ICF, namely, carbon nanofoams produced with the pulsed laser deposition (PLD) technique, by means of hydrodynamic numerical simulations. By comparison with a simulation of solid-density carbon, PLD nanofoams show a higher pressure at the shock front, which could make them potential good candidates as ablators for a capsule for direct-drive fusion.

1. Introduction

Porous materials, or foams, are the subject of an intense research activity in the context of inertial confinement fusion (ICF) and, more generally, of laser-matter interaction. Foams of low-Z elements have been proposed for use in ICF capsules, to generate bright X-ray sources [1], for the study of equations of state [2], and more recently for efficient electron acceleration [3].

In the context of ICF, foams are considered as constituents of the outer layer of the capsule, because of their ability to smooth the inhomogeneities in the laser energy [4–7], to enhance the laser absorption efficiency [8, 9], and to increase the ablation loading on a substrate [10]. These features make a foam ablator a potentially important choice to increase the laser-target coupling, thus transferring the laser energy into compression of the inner layers of the capsule.

Most of the experimental data available regard plastic foams, whose internal structure is constituted by features in the micrometric scale, such as filaments and membranes.

Typically, these foams are produced by chemical methods. However, the investigation of the behavior of porous materials constituted by different elements and materials is needed to explore other potential applications. Recent studies [11, 12] indicate the advantages of using mid-Z ablators, which can reduce the impact of laser plasma instabilities (LPIs), therefore increasing the performance of the target. Among them, high-density carbon (HDC), typically used in indirect-drive experiments, can be beneficial for enhancing the performances of capsules, not only for the indirect-drive scheme but also for the direct-drive approach. In this context, low-density carbon nanofoams could potentially combine the benefits coming from the use of an ablator made of mid-Z elements and from the features of plasma behavior deriving from its random internal structure.

In this work, we present the first numerical investigation of the behavior of nanostructured carbon foams produced with the pulsed laser deposition (PLD) technique [13–15] under the action of a high-power nanosecond-long laser beam, at conditions relevant to ICF. PLD nanofoams have

already been studied in the framework of high-intensity laser-matter interaction as a near-critical layer in double-layer targets [16] for ion acceleration with ultrafast lasers (pulse duration from ∼ 30 fs to 100s fs) [17, 18].

In this context, a solid theoretical understanding of the physical processes granting an enhanced acceleration has been developed thanks to particle-in-cell kinetic simulations [19–21], and the optimal nanofoam parameters (namely, thickness and density) have been determined as a function of laser intensity [22]. However, there are significant differences in the laser parameters between typical ultrafast laser-driven acceleration and ICF experiments, especially in terms of pulse duration (typically from 30 fs to 100s fs for the former, few ns for the latter) and irradiance (typically 10^{18}–10^{22} W/cm^2 and 10^{14}–10^{15} W/cm^2, respectively), and dedicated studies are thus required. Particle-in-cell codes are not suited to simulate dynamical processes evolving on the longer timescales relevant for ICF (up to hundreds of nanoseconds).

Here, we use the hydrodynamic MULTI-FM code [23], validated with experiments on microstructured plastic foams [24], to simulate the behavior of the PLD carbon nanofoams. The need for a dedicated code has been confirmed in the last years since modeling the foam as an equivalent medium of the same density in the simulations proved to be unsatisfactory [6, 23]. The MULTI-FM code features a model for reproducing the laser absorption in the foam and the behavior of the laser-generated plasma, by taking into account the randomly arranged internal structure of the material.

We consider a set of different nanofoam parameters, which depend on the manufacturing process used and in particular on the time duration of the laser employed. From the simulations, we find that the shockwave in all the foams is significantly slower than in a homogeneous medium with the same density as the nanofoam, as expected from the studies with the plastic foams [24, 25]. Moreover, we find the indication that the pressure at the front of the shockwave is significantly larger than the one obtained in the equivalent homogeneous medium.

2. Methods

2.1. Materials. The carbon nanofoam presented in this work is produced by pulsed laser deposition (PLD), a physical vapour deposition technique that employs a pulsed laser to remove material from a target and deposit it on a substrate in a controlled gas atmosphere. If the background gas pressure is sufficiently high with respect to the energy of the ablated species, they can be slowed to a diffusive regime and aggregate while in flight, giving rise to porous, nanostructured, low-density films. In the case of carbon, what can be obtained are carbon nanofoams, nanoparticle-assembled films with a fractal-like morphology, whose basic constituents are nanoparticles with dimensions in the order of 10 nm and densities as low as a few mg/cm^3.

Two different deposition systems are employed, one exploiting a nanosecond duration laser (ns-PLD, conventional technique) and the other an ultrashort femtosecond laser (fs-PLD). The first is a Q-switched Nd:YAG laser (second harmonic λ = 532 nm), with 5–7 ns pulse duration, 1 J maximum pulse energy, 10 Hz repetition rate; the second is a Ti:sapphire-based CPA laser (Coherent Astrella, λ = 800 nm), ∼ 100 fs pulse duration, 5 mJ maximum pulse energy, 1 kHz repetition rate. As shown in previous work [15], the different laser pulse duration leads to very different ablation regimes and enables better control of the foam properties. Notably, carbon nanofoams with the same density and different spatial uniformity (i.e., different microscale homogeneity) can be obtained.

The PLD target is pyrolytic graphite, the laser incidence angle is 45°, and the distance between target and substrate is fixed at 7 cm. We set the fluence to 360 mJ/cm^2 for both techniques, obtained with 8 mm spot size (top hat) and 260 mJ for ns-PLD and 0.8 mm spot size (FWHM) and 2.6 mJ for fs-PLD. By suitably tuning the vacuum chamber pressure in the range from 50 to 200 Pa (argon is used as an inert gas), carbon nanofoams of different densities are obtained. Combining the effect of the pressure with the effect of the different techniques (ns-PLD and fs-PLD), four kinds of representative carbon nanofoam are produced, as shown in Table 1.

The nanofoam morphology is characterized with a field emission scanning electron microscope (SEM, Zeiss Supra 40) with 3–10 kV accelerating voltage. The microscope electron is also exploited to perform EDXS (energy-dispersive X-rays spectroscopy) on the foam samples and to obtain information about the elemental composition and average density. This is done through the EDDIE method [26]: a theoretical model of the electron transport in the film and substrate allows to retrieve the film mass thickness starting from the ratio between the respective X-rays line intensities. The nanofoam thickness is measured from the SEM cross-sectional images, and the density is obtained as their ratio.

The determination of the nanofoam pore size δ_0, one of the parameters needed for the foam model implemented in the MULTI-FM code, is not straightforward: contrary to most of the chemically produced foams, pulsed laser-deposited nanofoams are cluster-assembled and fractal, with disordered voids without a clear shape. One possibility is to estimate the average pore size with the characteristic uniformity scale length of the nanofoam, that is, the average distance between two adjacent high-density regions of the foam (or equivalently the distance between two less-dense regions, i.e., the void dimension). The EDDIE method can be used point-by-point on the samples to build mass thickness maps of the foams, and by performing a Fourier transform analysis on the maps, the nanofoam uniformity scale length is obtained. In principle, it would be possible to perform the Fourier transform analysis directly on the SEM images, but they would be affected by electronic effects and arbitrary postprocessing (i.e., contrast and brightness), while the mass thickness maps cleanly convey the useful physical information. The structure factor $S(q)$ is the radius-averaged squared Fourier transform of the mass thickness image, and since the spatial frequency

TABLE 1: The parameters of the materials produced with the PLD. The solid element density ρ_s is taken as 2.0 g/cm^3 for all samples.

Series	Deposition method	Density ρ_p (mg/cm^3)	δ_0 (μm)	b_0 (nm)
A	ns-PLD	6	10	30
B	fs-PLD	6	20	60
C	ns-PLD	18	5	45
D	fs-PLD	18	10	90

q_{max}—corresponding to the maximum value of $S(q)$—is the predominant spatial frequency in the image, its inverse ($1/q_{max}$) is the uniformity scale length [15], and that value is used as an estimate for δ_0.

Four distinct categories of carbon nanofoams are produced and investigated in this work, as reported in Table 1: sample Figures 1(a) and 1(b) have a density of 6 mg/cm^3, which is the characteristic lowest carbon nanofoam density achievable with the PLD technique; sample Figures 1(c) and 1(d) are three times as dense (18 mg/cm^3), close to the highest density conditions in which the material retains a porous, foam-like structure. For each density, the samples produced with ns-PLD (Figures 1(a) and 1(c)) present a pore size that is half of the value obtained for corresponding fs-PLD samples (Figures 1(b) and 1(d)). This can be appreciated from Figure 1: Figures 1(a) and 1(d) are similar in the distance between two crests of the microscale foam structure, and Figure 1(b) has a greater spacing while Figure 1(c) is significantly more uniform. Figure 2 shows the respective EDXS mass thickness maps, highlighting the same nanofoam microstructure. From the Fourier transform image in the insets, the ring at q_{max} can be appreciated (note the wider scale for the Figure 1(c) inset).

Since carbon nanofoams grow through the random stacking of aggregates which are fractal in nature, it is possible to relate the density of the nanofoams to the characteristics of the fractal aggregates [15]:

$$\frac{\rho_p}{\rho_s} = k\left(\frac{d_{np}}{2R_g}\right)^{3-D_f}, \tag{1}$$

where ρ_p and ρ_s are, respectively, the foam and the solid element (nanoparticle) density and k is a proportionality factor related to the packing of the aggregates in the tridimensional foam structure. d_{np}, R_g, and D_f are the fractal aggregates properties: nanoparticle diameter, gyration radius, and fractal dimension. Since all the carbon nanofoams considered in this work have a fractal dimension $D_f \approx 2$ [15],

$$\frac{\rho_p}{\rho_s} = k\left(\frac{d_{np}}{2R_g}\right) = \left(\frac{d_{np}}{2R_g/k}\right). \tag{2}$$

The foam model implemented in the MULTI-FM code is still based on a fractal description but expresses the ρ_p over ρ_s ratio as a function of different parameters: the thickness of the solid elements b_0, the pore size δ_0, and the fractal parameter α.

$$\frac{\rho_p}{\rho_s} = \left(\frac{b_0}{\delta_0}\right)^{1/\alpha}. \tag{3}$$

By comparing the two equations, one could seek a way to express each term of (3) as a function of the parameters of the other, namely, d_{np}, $2R_g$, and D_f, since the left-hand term is the same in both equations. Given the number of parameters and their possible combinations, a complete term-by-term correspondence is not univocal. A very straightforward relationship between α and D_f can be derived, as they are both a measure of the fractality of the system, and it is reasonable to assume they should be independent of the other parameters. Under this hypothesis, equating the exponents of the two equations leads to $\alpha = (3 - D_f)^{-1} \approx 1$. Then, since the pore dimension δ_0 is obtained from the Fourier analysis of the mass thickness maps, the only remaining parameter b_0 can be calculated by inverting (3): $b_0 = ((\rho_p/\rho_s) \cdot \delta_0)^{\alpha} = (\rho_p/\rho_s) \cdot \delta_0$. A value of 2.0 g/cm^3 is taken as solid element density ρ_s, coherent with the disordered sp^2 structure of the carbon nanoparticles composing the nanofoam [13, 14, 27]. The main parameters for the different carbon nanofoams considered in this study (Series A, B, C, and D) are shown in Table 1: their density, pore dimension δ_0, and solid element dimension b_0, along with the respective production technique (ns- or fs-PLD). It can be noted that the value of the solid element thickness b_0, in the order of some tens of nanometers, is coherent with the foam microstructure as seen in high magnification SEM images. Since the nanoparticle diameter is around 10 nm, the carbon nanofoam solid element can be identified with the strands of connected nanoparticles that make up the short-range structure of the nanofoams, which delimit the voids—of dimension δ_0—from one another. Therefore, the foam model implemented in MULTI-FM is representative of the nanofoam microstructure, while it is not sensitive to the short-range nanostructure (namely, the nanoparticles composing the foam solid element).

2.2. MULTI-FM Simulations. We simulated the behavior of the laser-generated plasma with the 1D MULTI-FM code [23]. The MULTI-FM code is a modification of the MULTI code [28] specifically developed for reproducing the interaction of powerful laser pulses with porous materials. It is based on an effective model for laser absorption accounting for the effect of solid elements and empty spaces on the plasma behavior. In the model, the pore size δ_0, the thickness of the solid elements b_0, the average density of the foam ρ_p, and the density of the solid parts ρ_s are related as in equation (3). In the code, the homogenization status of the plasma is determined through a parameter called ISFOAM, defined for each numerical cell at each time step as

$$\text{ISFOAM}(x,t) = 1 - \frac{H(x,t)}{H_c}. \tag{4}$$

In this equation,
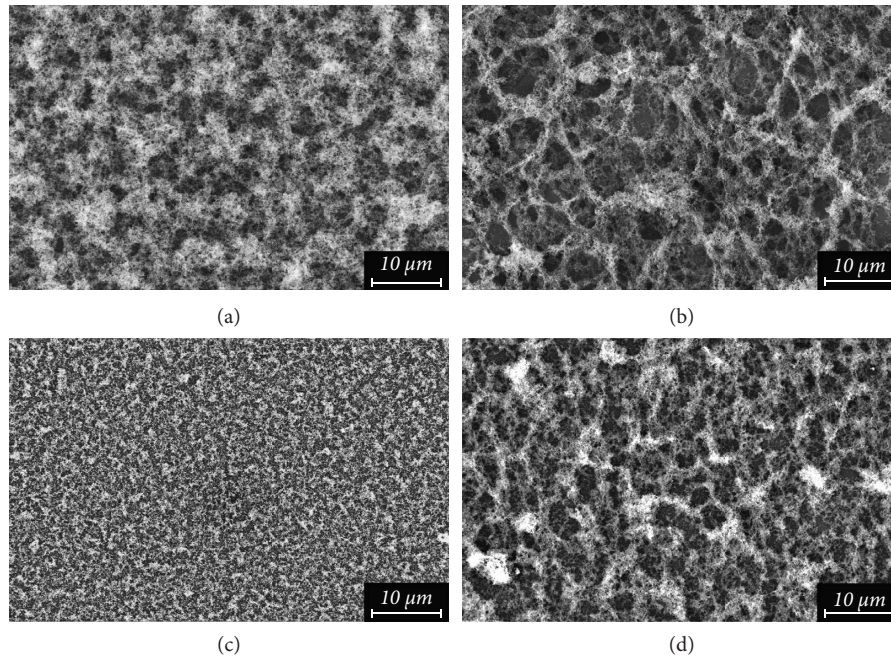
Figure 1: SEM micrographs of the carbon nanofoams produced. The respective properties can be found in Table 1 for the (a), (b), (c), and (d) samples. The images can be directly compared since the magnification is the same in all cases.
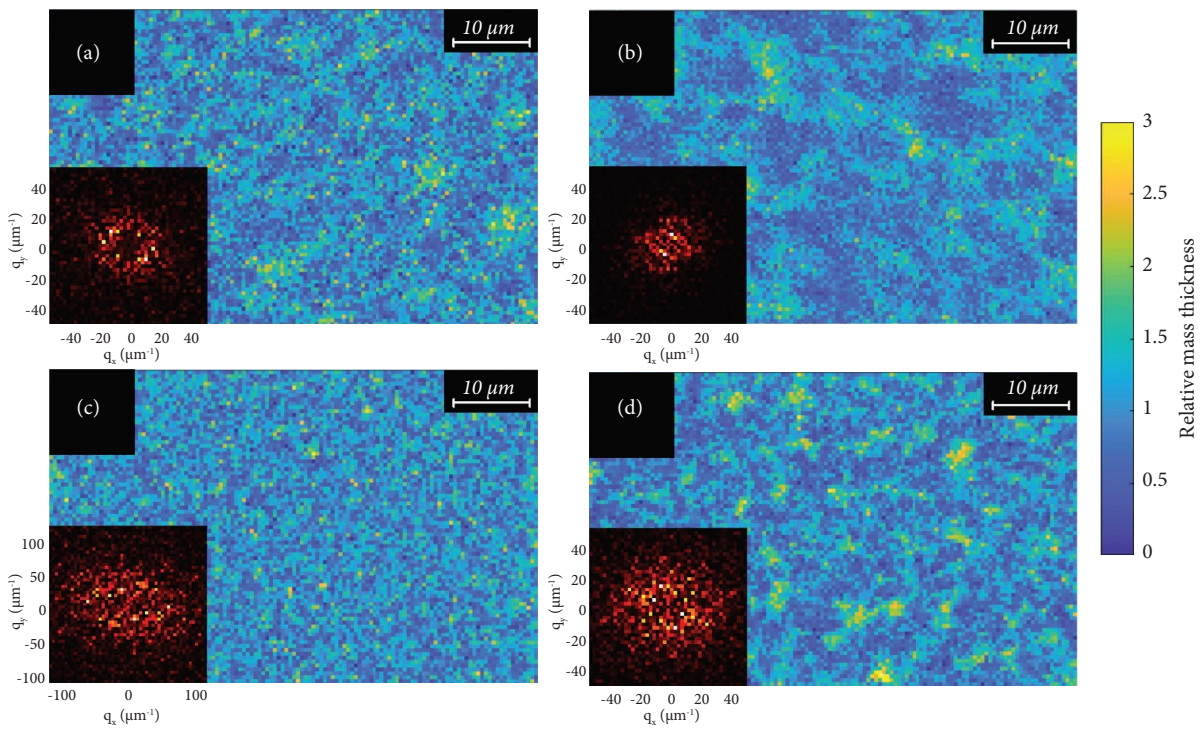
Figure 2: Mass thickness maps of the carbon nanofoam samples from Figure 1. In the inserts on the lower left, the Fourier transform of the respective image is shown. The anticorrelation between uniformity scale and maximum q can be appreciated (note the different scale of the inset of figure (c)).

$$H(x,t) = 2 \int_0^t \frac{dt'}{\tau_H\left(x,t'\right)}, \tag{5}$$

where τ_H is the characteristic homogenization time given as follows:

$$\tau_H \approx 2.4 \cdot 10^{-3} \frac{Z^4 \left(\delta_0 - b_0\right)^2 \rho_p}{A^{(1/2)} T^{(5/2)}}$$

$$= 2.4 \cdot 10^{-3} \frac{Z^4 \delta_0^2 \left[1 - \left(\rho_p/\rho_s\right)^\alpha\right]^2 \rho_p}{A^{(1/2)} T^{(5/2)}}, \tag{6}$$

where Z is the effective ionization, A is the mass number, and T is the temperature of the plasma. In the last step, equation (3) was substituted in place of b_0 to better illustrate the dependence of the homogenization time on pore dimension and density. Due to the low density of the nanofoams, $(\rho_p/\rho_s) \ll 1$, therefore, $\tau_H \propto \delta_0^2 \rho_p$. When the homogenization is reached, $H(x,t_h)$ is

$$H(x,t_h) = H_c = \begin{cases} 1, & \rho_p \geq \rho_c, \\ \\ 1 - \left[\dfrac{1 - \left(\rho_p/\rho_c\right)^\alpha}{1 - \left(\rho_p/\rho_s\right)^\alpha}\right]^2, & \rho_p < \rho_c. \end{cases} \tag{7}$$

As the plasma is heated and homogenized, the parameter ISFOAM changes from 1 for the cold, not yet irradiated foam, to 0, when the plasma in the cell is completely homogenized. In the model, the thermal conduction is limited by the same parameter ISFOAM, to account for the inhomogeneous distribution of free electrons in the pores during homogenization as follows:

$$q(x,t) = -(1 - \text{ISFOAM}(x,t))\left[\chi(x,t)\frac{\partial T_e}{\partial x}\right], \tag{8}$$

where $q(x,t)$ is the heat flux, $\chi(x,t)$ is the Spitzer conductivity, and $T_e(x,t)$ is the electron temperature. In the same fashion, the force acting on the mesh nodes is limited by the homogenization as

$$\frac{\partial v}{\partial t} = -(1 - \text{ISFOAM}(x,t))\frac{\partial P}{\partial m}, \tag{9}$$

where $v(x,t)$ is the node velocity, $P(x,t)$ is the total pressure, and m is the Lagrangian coordinates used in the calculations in the code.

The MULTI-FM code has been validated with an experimental campaign carried out at the ABC laser facility [24].

Here, the laser parameters are taken as the ones of the ABC laser facility, in view of an experimental campaign to be conducted there in the near future. The laser pulse has a $\sin^2$ temporal profile with a full-width half maximum (FWHM) $\tau_L = 3$ ns, at the fundamental wavelength $\lambda_L = 1054$ nm, with an intensity on target of 10^{14} W/cm^2. The parameters for the carbon nanofoam samples used in the simulations are

the ones indicated in Table 1. In all the simulations, a tabulated equation of state from the SESAME library has been used. The carbon ions are considered to be fully ionized, $Z_{\text{eff}} = 6$. For all the simulations, the thickness of the sample has been taken as $300\,\mu$m, the largest possible to obtain by PLD in a reasonable production time.

3. Results

We report a series of simulations performed with the MULTI-FM code. The foam parameters have been chosen as the ones reported in Table 1. We will refer to each simulated nanofoam sample with the corresponding series name reported in that table. As explained in the Methods section, the laser wavelength in the simulations is taken as $\lambda_L = 1054$ nm. The corresponding critical mass density is, therefore, 3.3 mg/cm^3, which means that all the foams we are considering are overcritical.

Figure 3 shows the results of the simulations for Series A and B, having both the density of 6 mg/cm^3 and the pore size of 10 and $20\,\mu$m, respectively. The shockwave in the nanofoam is slower than in the homogeneous medium. This behavior is well known and theoretically and experimentally documented in the literature for plastic foams [5, 6, 23–25, 29]. It is due to the time required for the laser-generated plasma to homogenize and fill the empty spaces in the foam. The lack of free electrons and the inhomogeneity of the plasma lead to a reduced heat conduction and hydrodynamic motion, until the plasma is homogenized. At that point, the plasma behaves as an ordinary homogeneous plasma.

The characteristic time of homogenization is affected by the pore size δ_0 as in (6). Because of this dependence, the homogenization time is increased in the case of the nanofoams of Series B, compared to the ones of Series A, and the shockwave is slower in the former than in the latter.

The plots on the right column show that the pressure of the plasma attained in the foam is noticeably higher than that one obtained in the homogeneous medium of the same density. As analytically demonstrated in Ref. [7], an overcritical foam is more efficient than a solid homogeneous material in converting the laser energy into ablation loading. The lower thermal conduction and the inhibited hydrodynamic motion of the cold part of the foam lower the fraction of the laser energy absorbed into the plasma converted into compression or heating of the material. Therefore, a large fraction of this energy is left in the plasma as thermal energy, increasing the pressure in the foam. This property of the foam plasma can be relevant for ICF because it will increase the efficiency of compression on the first inner layer in the fusion target. This feature of foams will be beneficial for ICF, especially considering also the other properties of foam materials, the most important being the high absorption efficiency of the laser energy, which can be as high as 90%.

Figure 4 shows the results of a simulation of a solid-density carbon sample obtained with the MULTI code and with the same equation of state used for the foams, and the density is equal to 2.0 g/cm^3. The pressure at the shock front

Figure 3: The simulations for the homogeneous material and for the nanofoams of cases A and B as in Table 1. The homogeneous material has the same density as the average density of the A and B. The laser comes from the right.

Figure 4: The results of simulations with the MULTI code for the case of a sample of solid carbon. The laser comes from the right.
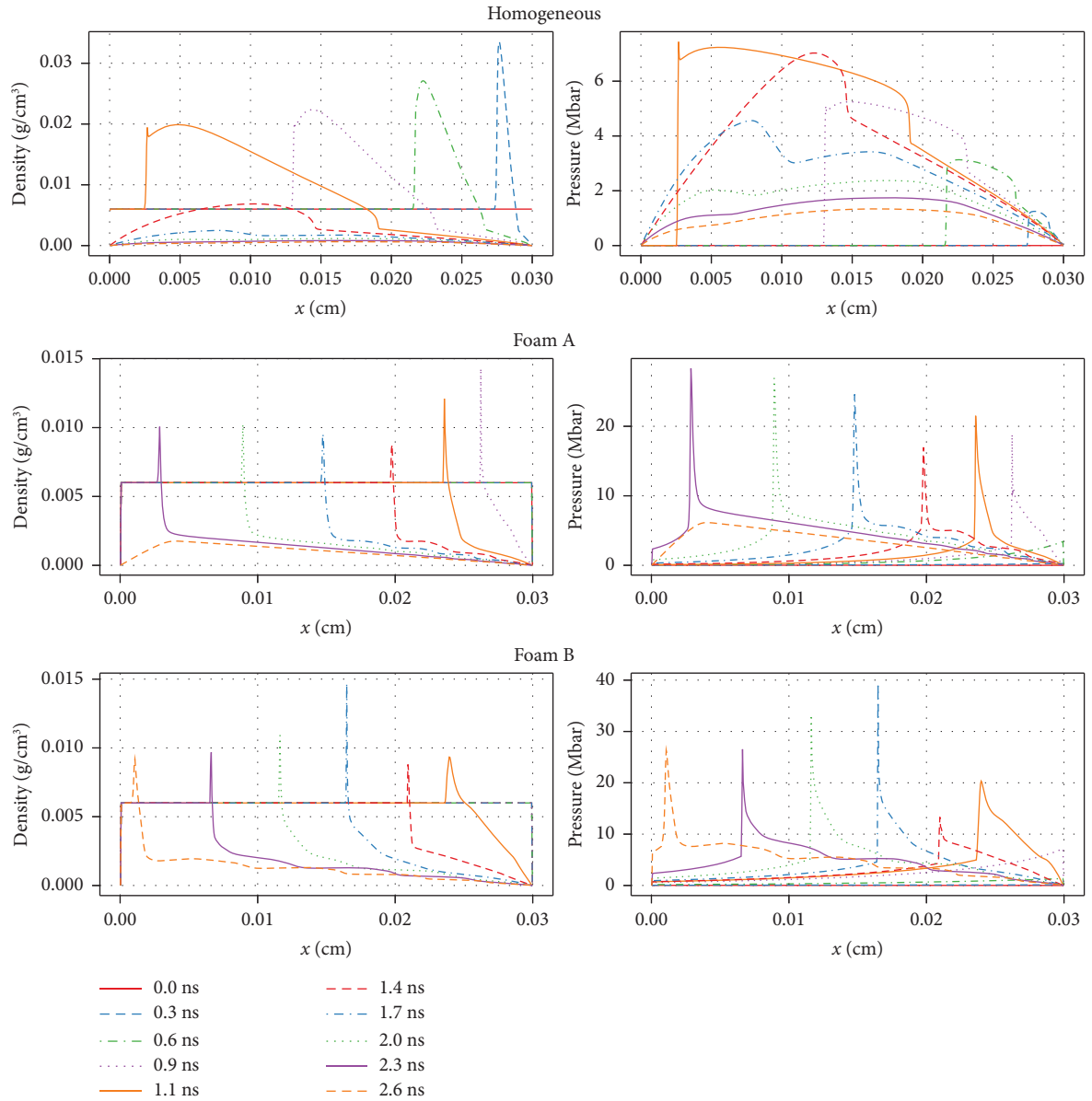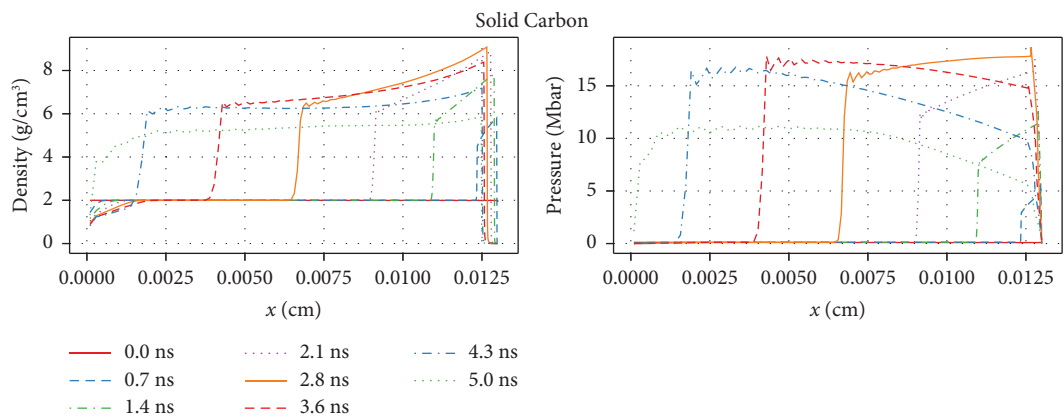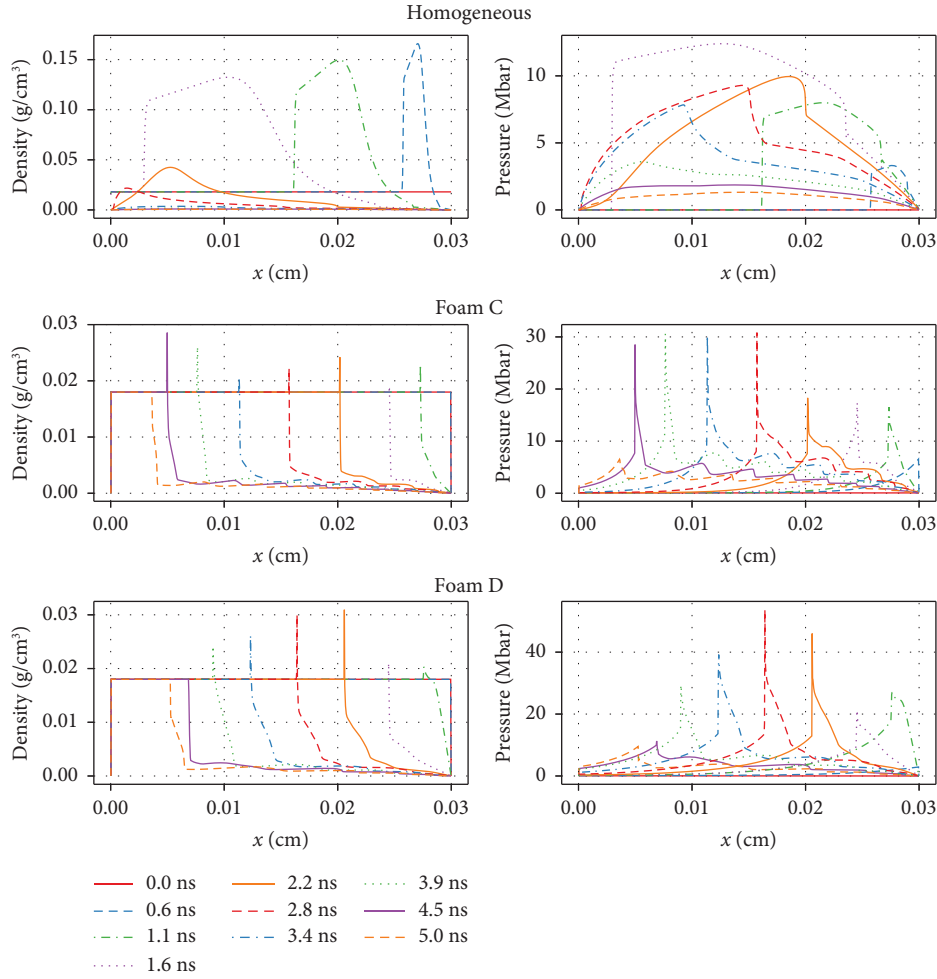
FIGURE 5: The simulations for the homogeneous material and for the nanofoams of cases C and D as in Table 1. The homogeneous material has the same density as the average density of the C and D nanofoams. The laser comes from the right.

in the nanofoam Series A exceeds the pressure obtained in the diamond sample. This effect is even more evident in the case of the nanofoam Series B, where on average it exceeds 20 Mbar.

Figure 5 shows the results of the simulations performed with the nanofoams Series C and D. The oscillations which can be seen in the plots of the density and pressure, in the plasma behind the shock front, are due to the interplay between the homogenization of the plasma and the propagation of the shockwave during the simulation. They reflect the inhomogeneous nature of the plasma realized inside the foam, where some inhomogeneities on large scales are known to remain long after the homogenization time [30]. In nanofoams Series C and D, the shockwave in the foam is slower than in the case of Figure 3. The pore size is smaller, leading to a reduction in the homogenization time, but, at the same time, the density is increased, with the opposite effect (see (6)). The homogenization time is thus mostly unchanged, and the slower shockwave propagation can be attributed to the higher density of the material. The pressure at the shock front in the nanofoam Series C exceeds 20 Mbar on average, an effect even more noticeable in Series D, where it exceeds 30 Mbar.

These results show how a foam can improve the ablation loading, by giving a higher pressure at the front of the shock wave compared with a homogeneous medium. The foams show in all cases a first narrow peak of the pressure at the shock front, followed by a thicker zone of pressure which has generally the same value attained in the homogeneous material. This behavior is related to the limiters in the model, which act on the thermal conductivity and on the compression of the material, reducing both effects (see (8) and (9) in Ref. [23]). The fraction of the plasma energy transformed into the motion of the fluid, and the one transported by heat conduction is reduced in comparison with a homogeneous medium, leading to an increase in the pressure at the front of the shock, which travels at a lower speed.

The simulations can also give an estimate of the most effective choice for the thickness of the sample, to maximize the pressure at the shock front when it exits the ablator. While for Series A, the highest pressure is attained at the end of the laser pulse, in Series B, the peak pressure is reached at 1.7 ns, before the peak power of the laser. By looking at Series C and D, we see that the peak pressure is always reached at about half of the laser time, i.e., when the laser is at its maximum power. Therefore, by properly choosing the

thickness of a carbon nanofoam ablator, depending on the specific laser temporal profile, one can increase the pressure at the shock front and maximize the ablation loading, analogously to what has been observed in Ref. [7] for plastic foams. When considering carbon nanofoams of 18 mg/cm^3, for both Series C and D, a thickness of the sample of about 150 μm would be the optimal to improve the compression efficiency from the ablator. Samples with this thickness can easily be obtained with the PLD technique. We will perform dedicated experiments on the ABC facility in the near future to characterize the laser-generated plasma with these nanofoams and to test the results obtained with the MULTI-FM code described in this work.

4. Conclusion

In this work, we reported a first study on the use of carbon nanofoams obtained with the pulsed laser deposition technique as ablators for ICF experiments. We considered four kinds of samples obtained through the use of nanosecond and femtosecond pulsed lasers, reported in Table 1. Taking advantage of the flexibility provided by the two different PLD techniques, two pairs of carbon nanofoams samples with the same average density but different microscale structures (and thus pore size) have been produced: samples A and B with a density of 6 mg/cm^3 and C and D of 18 mg/cm^3. Samples A and C, produced with ns-PLD, have smaller pore size, while larger pore size is obtained for samples B and D, produced with fs-PLD. The nanofoams are characterized in terms of morphology, and a connection between the fractal nanofoam model [15] and the foam description implemented in the MULTI-FM code is proposed. We investigated the behavior of these samples under irradiation of a high-power laser by numerical simulations performed with the MULTI-FM code. In particular, we considered the laser parameters as one of the ABC laser facilities at ENEA Centro Ricerche Frascati. The simulations showed that the shockwave into the nanofoam propagates sensibly slower than in a homogeneous medium of the same average density because of the internal structure of the foam. This effect is enhanced in the case of the nanofoams of Series C and D with an average density of 18 mg/cm^3 due to the larger average density compared to Series A and B, having an average density of 6 mg/cm^3. In all the nanofoams, the pressure at the front of the shockwave is larger than the one obtained in the equivalent homogeneous medium and also higher than the one obtained in a compact carbon sample, whose behavior has been simulated with the same code and equation of state. These first simulations on compact carbon, while limited in scope, are preparatory for future development toward the study of HDC ablators, and the implementation of the proper equation of state into the MULTI-FM code is foreseen. This effect can be of use for realizing an ablator layer for a fusion capsule, increasing the ablation loading on a subsequent layer, thus increasing the compression efficiency. This can be important for direct-drive inertial fusion with carbon-based ablators, such as HDC ablators. Theoretical works showed that mid-Z ablators have a better overall performance than plastic ablators,

also reducing the LPI detrimental effects [12]. The use of carbon nanofoams could improve the performances of fusion targets, combining the benefits that can be obtained from a mid-Z ablator with the ones that come from the use of a porous material, such as the reduction of laser imprint and the smoothing of the laser energy on the capsule. A potential issue related to this finding could reside in the ability of the model implemented in the MULTI-FM code, which presently does not include the possible effects deriving from the interaction of the laser with the peculiar nanoscale structure of the material. Dedicated experiments are foreseen in the near future to confirm the results of this work, through an experimental campaign to be held at the ABC laser facility.

Data Availability

The data that support the findings of this study are available from the corresponding authors upon reasonable request.

Disclosure

Conflicts of Interest

The authors declare that they have no conflicts of interest.

Acknowledgments

References

[1] F. Pérez, J. R. Patterson, M. May et al., "Bright x-ray sources from laser irradiation of foams with high concentration of Ti," *Physics of Plasmas*, vol. 21, no. 2, Article ID 23102, 2014.

[2] D. Batani, A. Balducci, W. Nazarov et al., "Use of low-density foams as pressure amplifiers in equation-of-state experiments with laser-driven shock waves," *Physical Review*, vol. 63, no. 4, Article ID 46410, 2001.

[3] O. N. Rosmej, N. E. Andreev, S. Zaehter et al., "Interaction of relativistically intense laser pulses with long-scale near critical plasmas for optimization of laser based sources of MeV electrons and gamma-rays," *New Journal of Physics*, vol. 21, no. 4, Article ID 43044, 2019.

[4] S. Y. Gus'kov, N. V. Zmitrenko, and V. B. Rozanov, "The laser greenhouse thermonuclear target with distributed absorption of laser energy," *Journal of Experimental and Theoretical Physics*, vol. 81, no. 2, pp. 296–305, 1995.

[5] S. Depierreux, C. Labaune, D. T. Michel et al., "Laser smoothing and imprint reduction with a foam layer in the multikilojoule regime," *Physical Review Letters*, vol. 102, no. 19, Article ID 195005, 2009.

[6] P. Nicolaï, M. Olazabal-Loumé, S. Fujioka et al., "Experimental evidence of foam homogenization," *Physics of Plasmas*, vol. 19, no. 11, Article ID 113105, 2012.

[7] M. Olazabal-Loumé, P. Nicolaï, G. Riazuelo et al., "Simulations of laser imprint reduction using underdense foams and its consequences on the hydrodynamic instability growth," *New Journal of Physics*, vol. 15, no. 8, Article ID 85033, 2013.

[8] A. E. Bugrov, S. Y. Gus'kov, V. B. Rozanov et al., "Interaction of a high-power laser beam with low-density porous media," *Journal of Experimental and Theoretical Physics*, vol. 84, no. 3, pp. 497–505, 1997.

[9] M. Cipriani, S. Y. Gus'kov, F. Consoli et al., "Time-dependent measurement of high-power laser light reflection by low-Z foam plasma," *High Power Laser Science and Engineering*, vol. 9, p. e40, 2021.

[10] R. De Angelis, F. Consoli, S. Y. Gus'kov et al., "Laser-ablated loading of solid target through foams of overcritical density," *Physics of Plasmas*, vol. 22, no. 7, Article ID 72701, 2015.

[11] M. Hohenberger, D. T. Casey, A. L. Kritcher et al., "Integrated performance of large HDC-capsule implosions on the national ignition facility," *Physics of Plasmas*, vol. 27, no. 11, Article ID 112704, 2020.

[12] M. Lafon, R. Betti, K. S. Anderson et al., "Direct-drive–ignition designs with mid-Z ablators," *Physics of Plasmas*, vol. 22, no. 3, Article ID 32703, 2015.

[13] A. Zani, D. Dellasega, V. Russo, and M. Passoni, "Ultra-low density carbon foams produced by pulsed laser deposition," *Carbon*, vol. 56, pp. 358–365, 2013.

[14] A. Maffini, A. Pazzaglia, D. Dellasega, V. Russo, and M. Passoni, "Growth dynamics of pulsed laser deposited nanofoams," *Physical Review Materials*, vol. 3, no. 8, Article ID 83404, 2019.

[15] A. Maffini, D. Orecchia, A. Pazzaglia, M. Zavelani-Rossi, and M. Passoni, "Pulsed laser deposition of carbon nanofoam," *Applied Surface Science*, vol. 599, Article ID 153859, 2022.

[16] M. Passoni, F. M. Arioli, L. Cialfi et al., "Advanced laser-driven ion sources and their applications in materials and nuclear science," *Plasma Physics and Controlled Fusion*, vol. 62, no. 1, Article ID 14022, 2019.

[17] I. Prencipe, J. Metzkes-Ng, A. Pazzaglia et al., "Efficient laser-driven proton and bremsstrahlung generation from cluster-assembled foam targets," *New Journal of Physics*, vol. 23, no. 9, Article ID 93015, 2021.

[18] M. Passoni, A. Sgattoni, I. Prencipe et al., "Toward high-energy laser-driven ion beams: nanostructured double-layer targets," *Physical Review Accelerators and Beams*, vol. 19, no. 6, Article ID 61301, 2016.

[19] L. Fedeli, A. Formenti, C. E. Bottani, and M. Passoni, "Parametric investigation of laser interaction with uniform and nanostructured near-critical plasmas," *The European Physical Journal D*, vol. 71, no. 8, p. 202, 2017.

[20] L. Fedeli, A. Formenti, L. Cialfi, A. Sgattoni, G. Cantono, and M. Passoni, "Structured targets for advanced laser-driven sources," *Plasma Physics and Controlled Fusion*, vol. 60, no. 1, Article ID 14013, 2017.

[21] A. Maffini, F. Mirani, M. Galbiati et al., "Towards compact laser-driven accelerators: exploring the potential of advanced double-layer targets," *EPJ Techn Instrum*, vol. 10, no. 1, p. 15, 2023.

[22] A. Pazzaglia, L. Fedeli, A. Formenti, A. Maffini, and M. Passoni, "A theoretical model of laser-driven ion acceleration from near-critical double-layer targets," *Communications Physics*, vol. 3, no. 1, p. 133, 2020.

[23] M. Cipriani, S. Y. Gus'kov, R. De Angelis et al., "Laser-supported hydrothermal wave in low-dense porous substance," *Laser and Particle Beams*, vol. 36, no. 1, pp. 121–128, 2018.

[24] M. Cipriani, S. Y. Gus'kov, R. De Angelis et al., "Laser-driven hydrothermal wave speed in low-Z foam of overcritical density," *Physics of Plasmas*, vol. 25, no. 9, Article ID 92704, 2018.

[25] J. Velechovsky, J. Limpouch, R. Liska, and V. Tikhonchuk, "Hydrodynamic modeling of laser interaction with microstructured targets," *Plasma Physics and Controlled Fusion*, vol. 58, no. 9, Article ID 95004, 2016.

[26] A. Pazzaglia, A. Maffini, D. Dellasega, A. Lamperti, and M. Passoni, "Reference-free evaluation of thin films mass thickness and composition through energy dispersive x-ray spectroscopy," *Materials Characterization*, vol. 153, pp. 92–102, 2019.

[27] A. Maffini, A. Pazzaglia, D. Dellasega, V. Russo, and M. Passoni, "Production of carbon nanofoam by pulsed laser deposition on flexible substrates," in *Nanoporous Carbons for Soft and Flexible Energy Devices*, pp. 135–157, Springer, Berlin, Germnay, 2022.

[28] R. Ramis, R. Schmalz, and J. Meyer-Ter-Vehn, "Multi— a computer code for one-dimensional multigroup radiation hydrodynamics," *Computer Physics Communications*, vol. 49, no. 3, pp. 475–505, 1988.

[29] V. T. Tikhonchuk, T. Gong, N. Jourdain et al., "Studies of laser-plasma interaction physics with low-density targets for direct-drive inertial confinement fusion on the Shenguang III prototype," *Matter and Radiation at Extremes*, vol. 6, no. 2, Article ID 25902, 2021.

[30] J. Limpouch, V. T. Tikhonchuk, J. Dostál et al., "Characterization of residual inhomogeneities in a plasma created by laser ionization of a low-density foam," *Plasma Physics and Controlled Fusion*, vol. 62, no. 3, Article ID 35013, 2020.

Research Article

Helium as a Surrogate for Deuterium in LPI Studies

Matthias Geissel [ID]**, Adam J. Harvey-Thompson, Matthew R. Weis, Jeffrey R. Fein, David Ampleford, David E. Bliss, Aaron M. Hansen, Christopher Jennings, Mark W. Kimmel, Patrick Rambo, Jonathon E. Shores, Ian C. Smith, C. Shane Speas, and John L. Porter**

Sandia National Laboratories, Albuquerque, NM 87185, USA

Correspondence should be addressed to Matthias Geissel; mgeisse@sandia.gov

Helium or neopentane can be used as surrogate gas fill for deuterium (D2) or deuterium-tritium (DT) in laser-plasma interaction studies. Surrogates are convenient to avoid flammability hazards or the integration of cryogenics in an experiment. To test the degree of equivalency between deuterium and helium, experiments were conducted in the Pecos target chamber at Sandia National Laboratories. Observables such as laser propagation and signatures of laser-plasma instabilities (LPI) were recorded for multiple laser and target configurations. It was found that some observables can differ significantly despite the apparent similarity of the gases with respect to molecular charge and weight. While a qualitative behaviour of the interaction may very well be studied by finding a suitable compromise of laser absorption, electron density, and LPI cross sections, a quantitative investigation of expected values for deuterium fills at high laser intensities is not likely to succeed with surrogate gases.

1. Introduction

Many studies of laser-plasma interactions utilize gaseous targets to ensure volumetric heating rather than having the laser absorbed near a solid surface. In many of those experiments, the gas is hydrogen, or a combination of its heavier isotopes deuterium and tritium, since these elements are integral for the study of nuclear fusion processes. However, pure hydrogen fills can complicate experiments because of flammability, or the high pressure needed to generate the required density at room temperature. As a result, experimenters have chosen "surrogate" gases to facilitate experiments with minimal loss of fidelity. Those surrogates are chosen to either have high hydrogen content or to be physically (charge and mass) as close as possible to the ideal gas fill. One example is neopentane (2,2-dimethylpropane), which has been used in laser-plasma instability (LPI) studies over the years [1] because it provides a very high number of hydrogen atoms at normal atmospheric conditions with a minimum of carbon contamination. A neopentane gas fill is mostly used to avoid the complex and costly integration of cryogenics to achieve desired densities at a certain allowable pressure. Another example is helium, which is attractive as a deuterium molecule surrogate, since it has the same mass and charge until the molecules dissociate [2]. Identical electron densities are achieved at identical initial pressures and temperatures without the hazard of flammability, and helium is readily available in many laboratories.

Convenience, however, is gained at a cost. Hydrodynamics, laser absorption, radiation transport, LPI generation, and other parameters are influenced by the physical properties of plasma's constituents. Table 1 compares some of the physical properties of the optional gas fills.

The "Magnetized Liner Inertial Fusion" program (MagLIF) at Sandia National Laboratories [3, 4] prompted an extensive investigation of laser-plasma interactions for the applicable regime of densities and laser parameters [1]. Many inertial confinement fusion experiments use cryogenic fuel, which makes neopentane the preferred surrogate

because of the high density and low pressure at room temperature. However, MagLIF (to date) has generally used deuterium at moderate pressures and room temperature, favouring gas fills with helium as a surrogate for the initial experiments at Sandia because of the matching electron density at room temperature pressure. After obtaining a flammable gas permit for dedicated experiments that investigate laser-plasma interactions, the studies were extended to include scenarios with D_2, and comparisons between the different gases were accessible. The physical properties of a gas have an influence on the dynamics in creating a plasma and in the plasma's evolution. The following list describes a few properties that may affect laser-plasma interactions:

1.1. Multiplicity of Ion Species. Depending on density and temperature, different ion velocity distributions can lead to spatially varying ratios of ion species, affecting not only the average density but also the average median mass and nuclear charge, which in turn will affect the plasma through processes listed as follows. The formation of multispecies modes of ion-acoustic waves can also influence stimulated Brillouin scattering (SBS).

1.2. Molecular Mass. While the molecular mass is irrelevant as soon as the gas is ionized, it influences the initial pressure of a gas, and therefore, the initial conditions, since the thickness and deformation of the laser-entrance window, typically a few or submicron thick polymer film, depend on that pressure. This affects window absorption losses and the spatial distribution of the laser/plasma interface.

1.3. Ion Mass. The ion mass can affect the formation of ion-acoustic waves and therefore SBS. It also has a direct effect on sound speed, shock velocities, and rarefaction velocities. Therefore, it is essential to the density evolution of the plasma. The ion mass is also relevant for the formation of ion-acoustic waves and the magnitude of Landau damping, since the latter depends on the thermal ion velocity.

1.4. Nuclear Charge. Species with higher nuclear charge will have higher ion charge at a given temperature and density. The ion charge Z_i is a linear multiplier to the absorption coefficient in inverse bremsstrahlung absorption for the laser and directly affects laser heating. It is a dominant parameter for radiation transport and losses, which scale with Z_i^2 and influence how quickly the plasma reaches its final, intensity-determined temperature. Since temperature is also an important parameter for LPI, the nuclear charge may also influence LPI observables, such as SBS and stimulated Raman scattering (SRS) while the temperatures are still rising. Since, for most of the plasma volume, the phase of rising temperatures is much shorter than the time that the plasma is at the final temperature, the influence of nuclear charge on temperature is expected to be a subtle effect on LPI, if observable at all.

In the following sections, we will describe the physical principles that are affecting our observables, the setup of the experiments, an analysis of the results, and finally the conclusion.

2. Observables for the Interaction of Laser Light with Plasmas

Multiple processes occur while a laser pulse heats a plasma. In the case of MagLIF targets, a prepulse first hits a polyimide window which leads to an expansion of the heated window and to backscatter caused by SRS or SBS. After the window experiences some expansion, the main pulse of the laser further heats and penetrates the window plasma. With high densities and temperatures, the pressure of the window material may allow window plasma to mix with the gas fill [5]. SBS and SRS can be generated by the main pulse both from window plasma and fuel plasma as well as filamentation in the latter [2]. We assume that most of the LPI causes backscatter, but side scatter may occur. The fill gas is heated to plasma conditions, and with increasing density, temperature, and nuclear charge, radiation from the heated zone may heat colder regions of the gas. In the following sections, we will address individual physical processes during laser heating.

2.1. Stimulated Brillouin Scatter. SBS [6, 7] occurs when incident light transfers energy to an ion-acoustic wave, and it is expected predominately as backscatter, with a finite angular distribution that exceeds the cone angle of the incident, focused laser. While some SBS can happen in forward directions as well, the laser light will still be absorbed by the target and therefore contribute to the desired preheat. Forward scatter is not observable by the diagnostic suite presented in this study. In a homogeneous plasma, the growth rate for SBS is given by [8]

$$\gamma_0 = \frac{k_{iaw}eE}{4m_e\omega_0} \sqrt{\frac{Z_i\omega_p^2 m_e/m_i}{\omega_{iaw}\omega_s}}, \tag{1}$$

where k_{iaw}, ω_{iaw} are the wavenumber and frequency of the ion-acoustic wave, E, the electric field of the laser, e, m_e, the charge and mass of the electron, m_i, Z_i, the mass and charge state of the ion, and ω_p, ω_0, ω_s, the plasma frequency and the frequencies of the incident laser and the scattered wave. This dependency would suggest a decrease of SBS growth with the nuclear charge Z_0, since with increasing Z_0, the mass of an ion species grows faster than the charge state, particularly for relatively low temperatures resulting in partial ionization. However, the growth of SBS can be reduced by Landau damping [9], which is more effective for lighter ions. Here, the ion-acoustic wave transfers energy to ions, which move with velocities close to the wave's phase velocity. In general, the dominant ion-acoustic mode is expected to have a much faster phase velocity than any species' average thermal

TABLE 1: Comparison of important physical properties for H_2, D_2, DT, helium, and neopentane. It shall be noted that DT is technically a two-ion component plasma, but due to the minimal difference in mass, it behaves very similarly to a plasma with unique ion species, which cannot be assumed for neopentane.

Property	Hydrogen	DT	Deuterium	Helium	Neopentane
Advantage	Cosmic abundance	Ideal fusion fuel	Nonradioactive fusion fuel	Nonflammable	High normal density
Ion species	Unique	2-component	Unique	Unique	2-component
2-mean molecular mass	$2\ \mu$	$5\ \mu$	$4\ \mu$	$4\ \mu$	$72\ \mu$
Mean ion mass	$1\ \mu$	$2.5\ \mu$	$2\ \mu$	$4\ \mu$	$4.24\ \mu$
Mean nuclear charge	1	1	1	2	2.47

velocity. Therefore, plasmas with lighter ions, exhibiting a higher fraction of the Maxwell–Boltzmann velocity distribution near the wave's phase velocity, will experience stronger damping. For fusion-relevant plasmas such as those studied in this paper, a common ion temperature in the plasma is typically a valid assumption. As a result, a multispecies plasma will have multiple normal modes corresponding to isotope-specific thermal velocities [10]. These modes can compete and reduce SBS growth. Damping is particularly efficient for adding a (small) fraction of light ions to a heavier species, but the opposite has a potential for notable damping as well, specifically under the consideration of ion trapping [11].

2.2. Stimulated Raman Scatter.

Stimulated Raman scattering (SRS) [12] results from light transferring energy to an electron-plasma wave. Since electrons are several magnitudes lighter than ions, energy transfer is more efficient, and a scattered photon will be significantly red-shifted. The growth rate follows a similar pattern as SBS lowers the influence of charge state and mass ratio [8]:

$$\gamma_0 = \frac{k_{epw}eE}{4m_e\omega_0}\sqrt{\frac{\omega_p^2}{\omega_{epw}\omega_s}}, \tag{2}$$

where k_{epw} and ω_{epw} denote the wavenumber and frequency of the electron plasma wave. As apparent from (2), the influence of the ion properties for SRS can only be a secondary effect, such as mass flow, where densification and rarefaction of ion density cause a modification of the electron density on grounds of charge neutrality in the plasma. SRS *side scatter* can also occur if the incident laser light is s-polarized with respect to a strong, oblique density gradient [13]. Side scatter would only be observed if light is s-polarized with respect to the object plane, because it is unlikely that any feature can be discriminated from primary laser interactions if it is caused by light being scattered towards or away from the detector. SRS is more prevalent at densities between 10% and 25% of the critical density, n_c, for a given laser wavelength. Since the experiments discussed in this paper use fill densities below 10% n_c, SRS will likely be a small contributor to energy loss[1].

2.3. Laser-Target Coupling.

Coupling of laser energy into the gas is the primary objective of the laser preheat studies at Sandia, and the dominant process for laser deposition is absorption through inverse bremsstrahlung, characterized by the collisional absorption coefficient K [14]:

$$K = \frac{\nu_e\omega_p^2}{c\omega_0^2}\frac{1}{\sqrt{1 - \omega_p^2/\omega_0^2}}, \tag{3}$$

where ω_p is the plasma frequency, and ν_e is the electron collision frequency as described by [14]

$$\nu_e \propto \frac{n_e Z_i \ln \Lambda_e}{T_e^{3/2}}. \tag{4}$$

Equation (4) assumes that the collision frequency is much smaller than the plasma frequency, and $\ln \lambda_e$ is the weakly temperature- and density-dependant Coulomb logarithm. Z_i stands for the ion charge. It becomes immediately clear that different target gases affect heating via a different ion charge state Z_i as noted in the introduction. This brings up a dilemma for surrogate gases: unless you end up with an identical ion charge (such as using hydrogen instead of deuterium-tritium), it is impossible to match both electron density and absorption. As a result, either heating or LPI, or both, will not exactly reproduce the physics of the target gas to be modelled. A best-case compromise is to be found for meaningful studies.

Besides deposited energy, specific coupling details such as the total range of deposition (maximum laser propagation depth) and X-ray brightness distribution of the laser-heated channel can be used to identify similarities and differences for various experimental scenarios. In our experiments, we chose to reduce the density of helium targets by 10%, which we empirically found to preserve the propagation depth of the laser and therefore the plasma volume. Electron densities stay far below the critical density for the laser frequency when fully ionized. D_2 at room temperature and 60 psi against vacuum results in 5% n_e/n_c for 527 nm laser wavelength, while 54 psi of He leads to 4.5% n_e/n_c. Accordingly, no effects such as two-plasmon-decay, reflection at critical density, or enhanced absorption are expected.

2.4. Experimental Methods.

All of the experiments that have been evaluated for this study have been performed in the Pecos target area within the Z-Backlighter facility of Sandia National Laboratories. The Z-Beamlet laser [15] was used to heat a gas volume in a cylindrical target through a laser entrance hole that was covered with a thin polymer foil. A bird's eye view of the target area is depicted in Figure 1. Some experiments included additional diagnostics pictured in the figure, but this article will focus on the near-beam back-scatter imaging and shadowgraphy diagnostics.
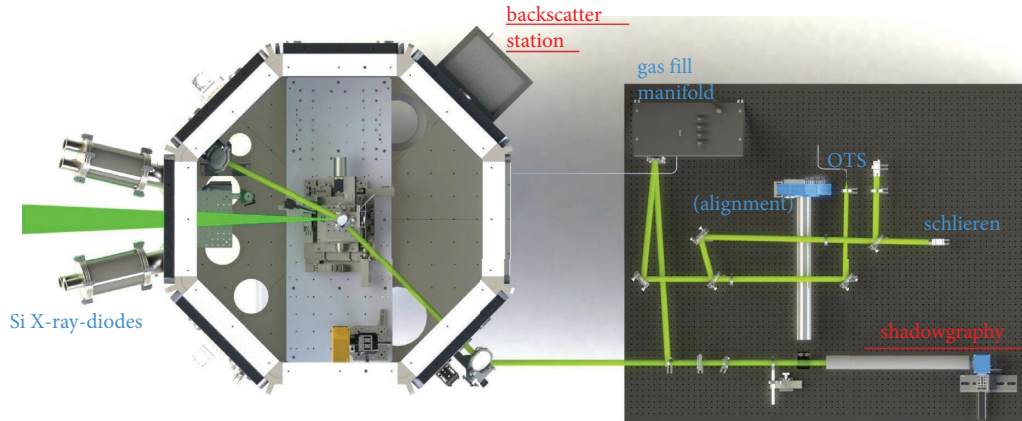
FIGURE 1: Bird's eye view rendering of the Pecos target area. Z-Beamlet (bright green) is entering from the left (north). A probe laser (soft green) is propagating through the target and analysed on an optical table to the right (south) of the target chamber.

The targets were cylindrical polycarbonate cells with a polyimide laser entrance window of 3 mm diameter and 1.7 μm thickness, assembled at Sandia by General Atomics [16]. The targets typically had four diagnostic ports. Two opposing ports with antireflective coated acrylic windows allowed the propagation of a probe beam for optical diagnostics, and two more ports enabled X-ray diagnostics via narrow slits. These slits were covered with 13 μm of polyester or polyimide to contain the fill gas. Figure 2 shows a rendering of the target cells. To protect optics and instruments inside of the target chamber, the gas cells were enclosed in a metal debris box, allowing only for the minimum required access to X-ray diagnostics. The optical diagnostic path was protected by secondary debris windows made from Duraplex™, an impact-hardened variant of polyacrylate [17].

2.5. LPI Diagnostics. The primary instruments for the observation of SBS in this paper are a photodiode filtered around the incident laser wavelength (526.6 nm) and a camera recording backscattered light with a similar filter. Both instruments measure the light that is reflected off a square polytetrafluoroethylene (PTFE) screen at the laser entrance wall of the experimental chamber, which has a central aperture that is just large enough to allow unimpeded propagation for the incident laser, as shown in Figure 3. Details for this setup without the diode, the near beam imager (NBI), were recently published by Geissel et al. [3] along with the calibration procedure. PTFE is commonly referred to by DuPont Corporation's product name *Teflon*™. With a thickness of a few millimeters, PTFE is an ideal diffuse reflector (scatterer) with an albedo in excess of 98% throughout the visible spectrum and more than 93% when including the near-infrared spectrum (up to $\lambda{\sim}2.5\,\mu$m) [18].

We observe SRS backscatter in a similar setup to SBS but with two differently filtered diodes (long pass filters at 610 nm and 710 nm). Indications of side scatter can be observed on shadowgraphy images of the interaction region as described as follows. Shadowgraphy is the main diagnostic for this observable, using the radial expansion dynamics of the laser-driven blastwave as an indicator for encircled

energy density. A detailed description of the measurement and evaluation of deposited laser energy in MagLIF targets has been published recently [19].

2.6. Shadowgraphy. A pulse train from the Chaco probe laser with a few millijoules at about 500 ps pulse length and 532 nm wavelength was used to image the propagation depth and shape of the laser-induced plasma channel. We will refer to each individual pulse as a frame to emphasize the imaging nature of the diagnostic and to distinguish it from the laser pulses of Z-Beamlet, which were the driver of the experiments. The probe propagation was orthogonal to Z-Beamlet. Two probe paths were used allowing an east-west view of the target in earlier experiments and an up-down view later. The Z-Beamlet laser was polarized horizontally and will, therefore, refer to the later setup as p-polarized view, since the laser polarization was parallel to the imaging plane. Adhering to standard optics terminology, we will refer to the earlier setup as s-polarized view. Figure 4 shows renderings of the p- and s-polarized setups including the two pinhole cameras for side-on and end-on X-ray imaging.

Up to four frames were used, with the late frames carrying blast wave expansion data for the determination of deposited energy. The earliest frame was typically within a few nanoseconds after the end of Z-Beamlet's main pulse, thus allowing us to determine the laser propagation depth and the overall shape of the heated region in the target. Only the first frame is used in this study. Later frames occurred with 25 ns separation between frames to improve the fidelity of energy deposition measurements as reported by Harvey-Thompson et al. [19]. The frames were recorded with an ultrafast hybrid CMOS detector developed at Sandia National Laboratories [20].

2.7. Laser Configurations. Z-Beamlet operates at the second harmonic (2ω) of Nd:YLF's 1053 nm line, which results in a centre wavelength of 526.6 nm. Pulses of 0.3–6 ns width can reach up to 1 TW power with a maximum contained energy of about 4.5 kJ, not accounting for losses in the subsequent beam transport. The laser beam with a square

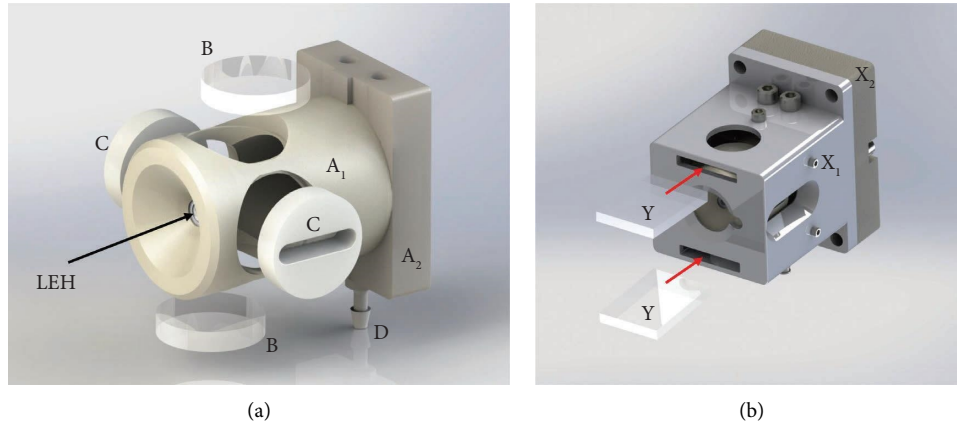(a)   (b)

FIGURE 2: (a) Exploded rendering of the target with the main body and mounting base (A1, A2), LEH, optical windows (B), X-ray diagnostic slits (C), and gas inlet nipple (D). (b) Debris enclosure with main body and base (X1, X2), and Duraplex™ debris windows (Y).

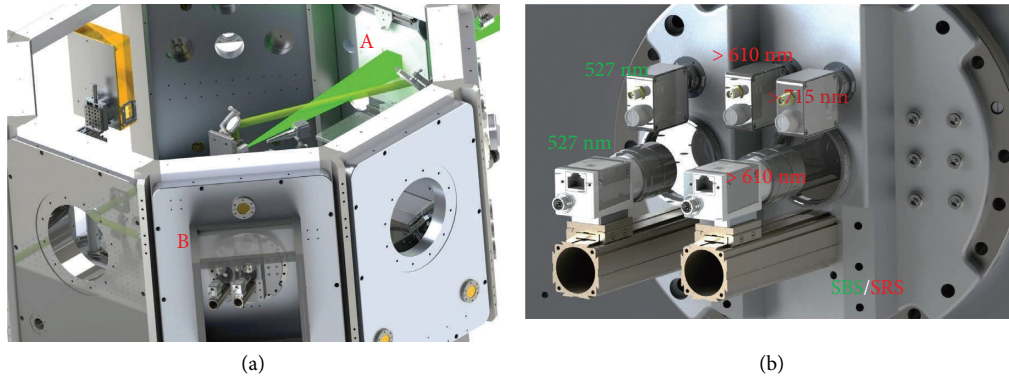
(a)   (b)

FIGURE 3: Setup of the SBS and SRS near-beam imaging diagnostics. (a) The Z-Beamlet laser enters the chamber through a hole in the PTFE screen (A). Backscattered SBS or SRS light illuminated the screen and recorded via filtered diodes and cameras in the NBI backscatter box (B). (b) Arrangement of instruments inside the NBI backscatter box.

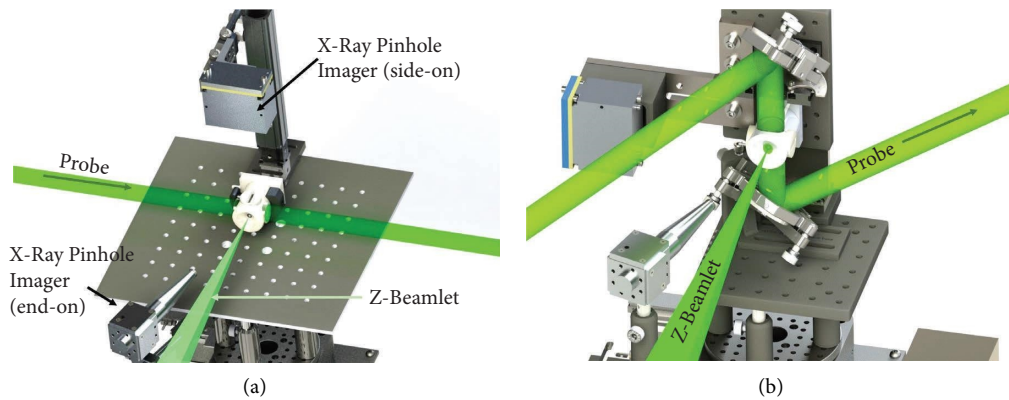(a)   (b)

FIGURE 4: (a) Configuration of the target chamber centre for s-polarized view with only one X-ray diagnostic port. (b) Configuration for the p-polarized view. The X-ray diagnostic port opposite to the pinhole camera is used for spectroscopy. Both renderings omitted to debris enclosure for better clarity.

cross section of 31 cm × 31 cm is focused by a 3.2 m lens onto the target with the best focus on the LEH window (with phase plate) or 3.5 mm in front of the LEH window (without phase plate). For the experiments described here, the laser energy was chosen not to exceed a total of 2.5 kJ on target. Three different laser configurations were chosen to reflect parameters that were historically relevant for MagLIF and covered different regimes of LPI generation.

Early experiments were used as a defocused spot on the LEH window without any spot smoothing by distributed phase plates (DPP [21, 22]). This scenario also used the highest power and ultimately yielded by far the highest LPI effects as described in detail in Geissel et al. [2]. As laid out in the same publication, two more configurations were employed by using phase plates with $750\,\mu m$ and $1100\,\mu m$ diameter for 95% of encircled energy in the spot, which we refer to as DPP750 and DPP1100. These two also used a longer main pulse with lower power to further reduce LPI without sacrificing laser energy. The area characterizing the peak intensity, not including the slopes of the focal spot's edges, was well described for either phase plate by a circle enclosing 75% of the laser energy [2] at $0.0025\,cm^2$ (DPP750) and $0.0053\,cm^2$ (DPP1100) but cannot be determined well for cases without phase plate. Acknowledging that concentrated areas with higher and lower intensities exist, we take the area of the smallest rectangle that encloses 75% of the energy as a substitute ($0.0013\,cm^2$). All laser configurations used a prepulse to preheat the LEH window and minimize its impact on the main pulse's energy deposition. The peak of this prepulse was set at 3.5 ns prior to $T = 0$, which is defined by the half-height point of the rising edge of the main pulse. Table 2 lists a summary of the laser configurations.

3. Results

Time-resolved data from the photodiodes consistently showed very different signatures for SRS versus SBS. The SBS diode shows a strong signal response for the prepulse, which most likely contains a significant contribution from laser reflection at the overdense window plasma. In contrast to SBS, the prepulse caused very little response in the SRS spectrum, and in most cases no measurable response at all. Also, the signatures in the SBS spectrum varied significantly for changing laser configurations. While shots without DPP showed the majority of the SBS in the main pulse, the shots with DPP successfully reduced SBS, mostly within the main pulse, which ended up creating less SBS than the prepulse. Figure 5 compares the diode traces of SBS and SRS for a shot without phase plate smoothing along with the SBS trace from a different shot that used a $750\,\mu m$ phase plate.

3.1. SRS Measurements. As expected from comparisons to literature and early NEWLIP simulations [2], the laser energy that is transferred to the Raman backscatter is very low. Estimates using the sensitivity and filter attenuation of the detectors along with a calibration at 527 nm wavelength resulted in values below 10 J even for the worst cases, though there is a large uncertainty in this estimate (>100%). Typical values should stay below one joule of backscattered SRS. The measured SRS seems unaffected by the laser spot size on target or the pulse length, but the measurements imply an exponentially growing dependence on the total laser energy. Figure 6 compares a number of experiments with and without phase plates for both helium and deuterium.

It is unclear why SRS would be growing nonlinearly with energy but be insensitive to intensity. A plausible explanation could be a combination of multiple effects: the strongly heated axial region of the target can create an electron density profile with focusing qualities, similar to the case of laser filamentation in dense gases [23]. Therefore, the propagation of the laser will no longer follow the original envelope associated with the focusing optics, and the size of the heated channel may depend on the overall power and heat conductivity, thus reducing the relevance of the focal spot area. Additionally, high intensities yield higher temperatures, causing a loss in SRS efficiency due to increased Landau damping and lower electron density (rarefaction). It is not surprising that the measurements are insensitive to the ion species, since neither the charge nor mass of the ion directly affect SRS, and the differences in density are within the error bars.

Side-scatter studies proved ambiguous at this time. Pronounced, transversal "wings" or flares in the shadowgraphs, which protruded further into the gas than one would expect from a blast wave, appeared frequently but only in an s-polarized view (see Figure 7 details). This could imply side scatter, and it is consistent with the polarization dependence of the side-scatter mechanism, but the phenomenon could not be reproduced reliably.

3.2. SBS Measurements. In contrast to SRS, the results for SBS are closer to what might be anticipated from first principles. Stimulated Brillouin scattering was observed strongest for unconditioned shots of high intensities as described by configuration 1 in Table 2. The fraction of SBS increases with intensity, and helium fills consistently yield more SBS than deuterium fills, which is expected due to higher Landau damping for deuterium. Figure 8 shows the data for SBS with configuration 1. Shots in helium tend to result in shorter propagation depths of the laser-heated region into the gas with increased total laser energy. This implies that SBS and other loss mechanisms increase so strongly that the additional pulse energy cannot compensate for the losses. This tendency is not pronounced for deuterium. Although the fraction of SBS losses in helium is higher by roughly 10 percentage points compared to deuterium, the propagation depth of the laser into the gas is similar to deuterium. This can be explained at least partially by the 10% lower fill pressure of the helium targets compared to deuterium.

The next lower-intensity scenario is configuration 2 of Table 1, using the $750\,\mu m$ wide phase plate. While the current dataset is not complete and lacks overlap between helium fills and deuterium fills in terms of total laser energy, it seems that helium fills yield less SBS reflectivity (~1% at 1.37 kJ and 2 kJ) than deuterium (6–8% at <1.35 kJ) as shown in Figure 7. An explanation for the SBS data could be that in this regime, Landau damping is no longer relevant, but the overall density is lower leading to less SBS. Higher laser energies led to shorter laser propagation in helium despite the low SBS values. At this time, we can only

Table 2: Comparison of laser configurations covered in this study including a plot illustrating the typical laser pulse train. $T = 0$ is defined as the half-height point of the rising edge of Z-Beamlet's main pulse. For more details about the focal intensity distribution with or without the two applied phase plates, see Geissel et al. [3].

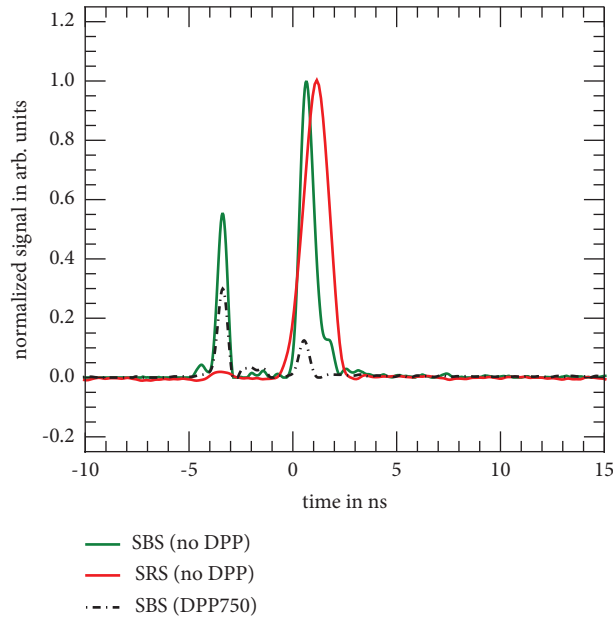| Config.	Phase plate	Prepulse energy (J)	Main pulse energy (J)	Main pulse width (ns)
1	—	350 ± 100	1600 ± 300	2
2	DPP750	120 ± 50	1400 ± 300	3.5
3	DPP1100	150 ± 100	1200 ± 500	3.5

Figure 5: Comparison of SRS and SBS traces for a shot without phase plate next to a trace from a shot with DPP750. The signals for the no-DPP shot are normalized peak at 1.0, while the DPP750 trace is scaled in proportion to its no-DPP counterpart.
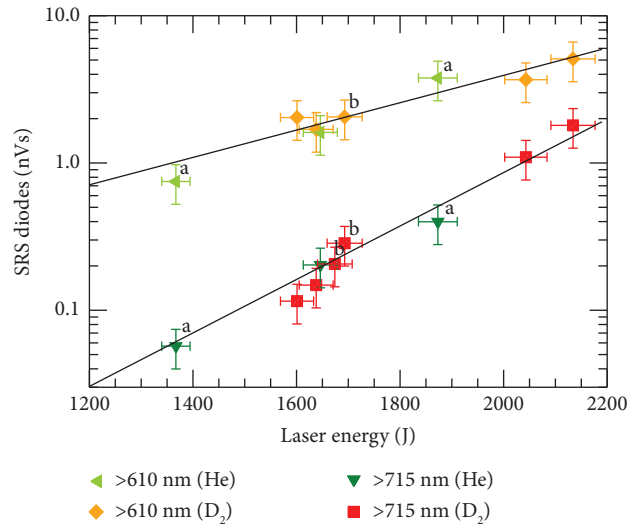

Figure 6: SRS backscatter data for He and D_2. Experiments were performed without DPP unless marked (a: DPP750 and b: DPP1100). Pulse shapes followed the configuration recipe given in Table 2. The black lines represent exponential fits.

speculate that additional LPI caused this effect. Such losses could be SRS or side scatter. The latter might be observable as conical "wings" in the first shadowgraphy frames (directly after the end of the heating laser pulse), which are inserted in Figure 7. As mentioned in the SRS results section, such wings can be observed frequently for experiments with high-to-medium LPI in s-polarized view (see Figure 4).
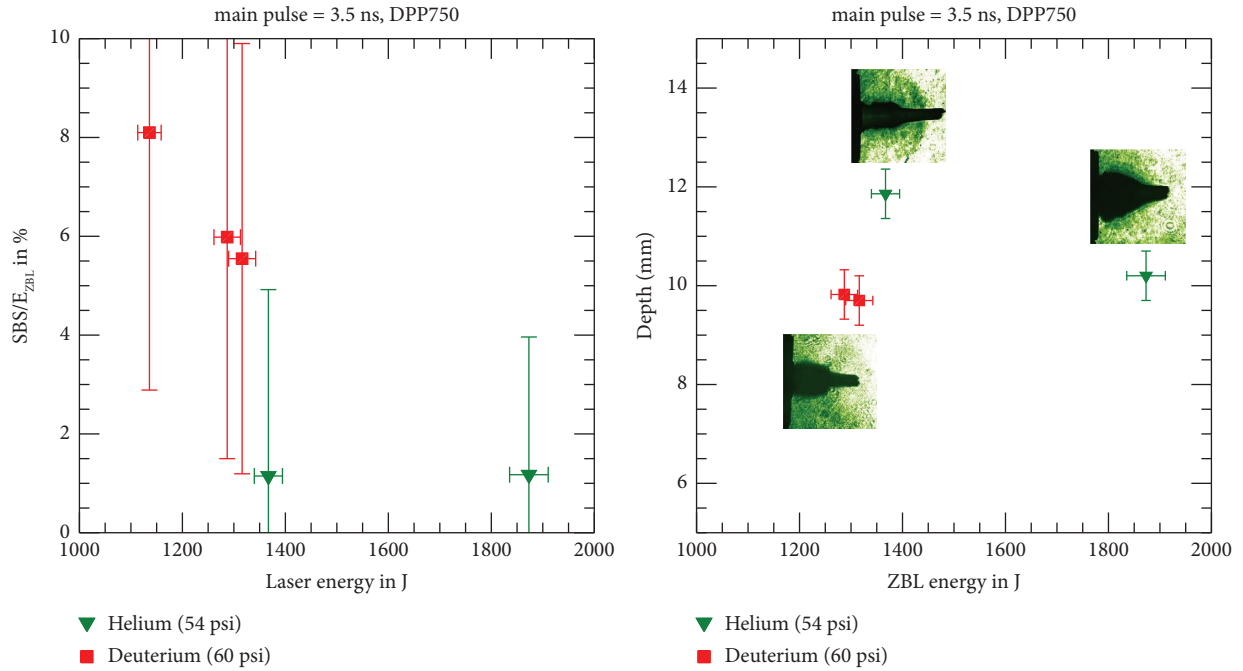
FIGURE 7: Dataset for laser shots with configuration 2 from Table 2. Note that a depth data point for deuterium is missing due to diagnostic malfunctions. The depth plot includes shadowgraph inserts with the laser entering from the right and the blast wave casting a dark shadow.
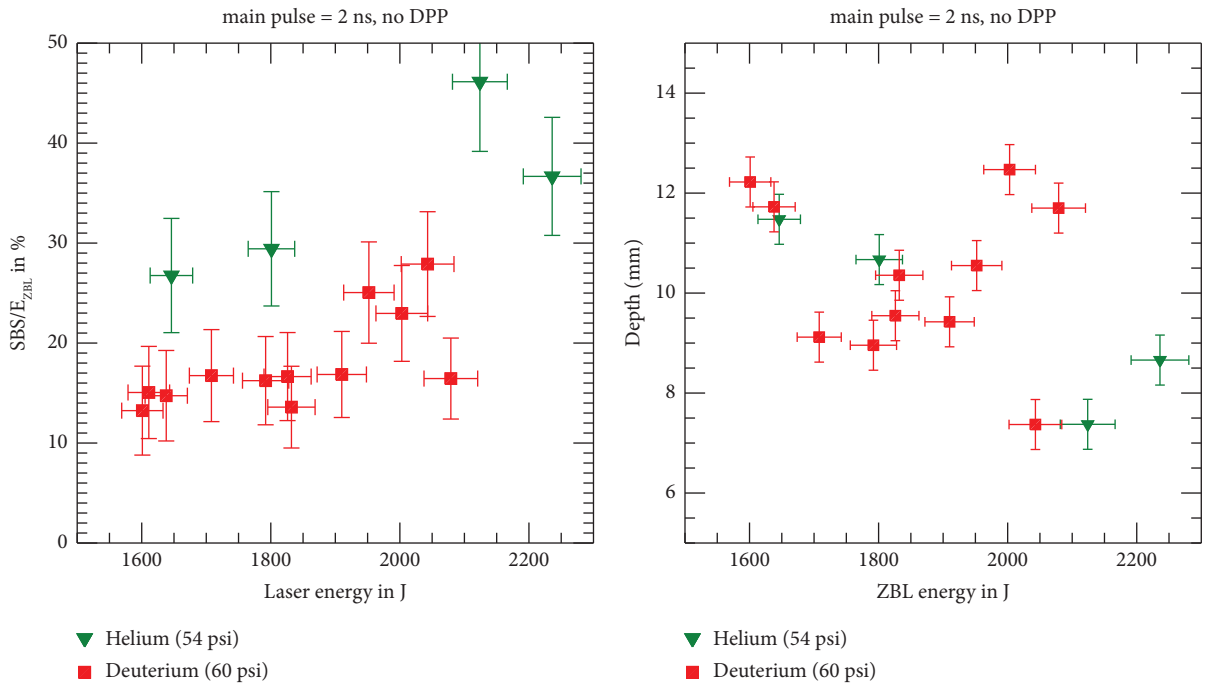

FIGURE 8: Dataset for laser shots using configuration 1 from Table 2.

The lowest intensities (configuration 3) with an $1100 \, \mu m$ diameter phase plate almost eliminated SBS, and no measurable difference between helium and deuterium can be seen, which is plotted in Figure 9. Also, laser propagation depth increases almost linearly with laser energy. A good approximation is a depth increase following $E_{las}^{0.75}$, which is not too far from basic absorption wave propagation estimates of $\sim E_{las}^{0.6}$ for a given pulse length [14, 24].
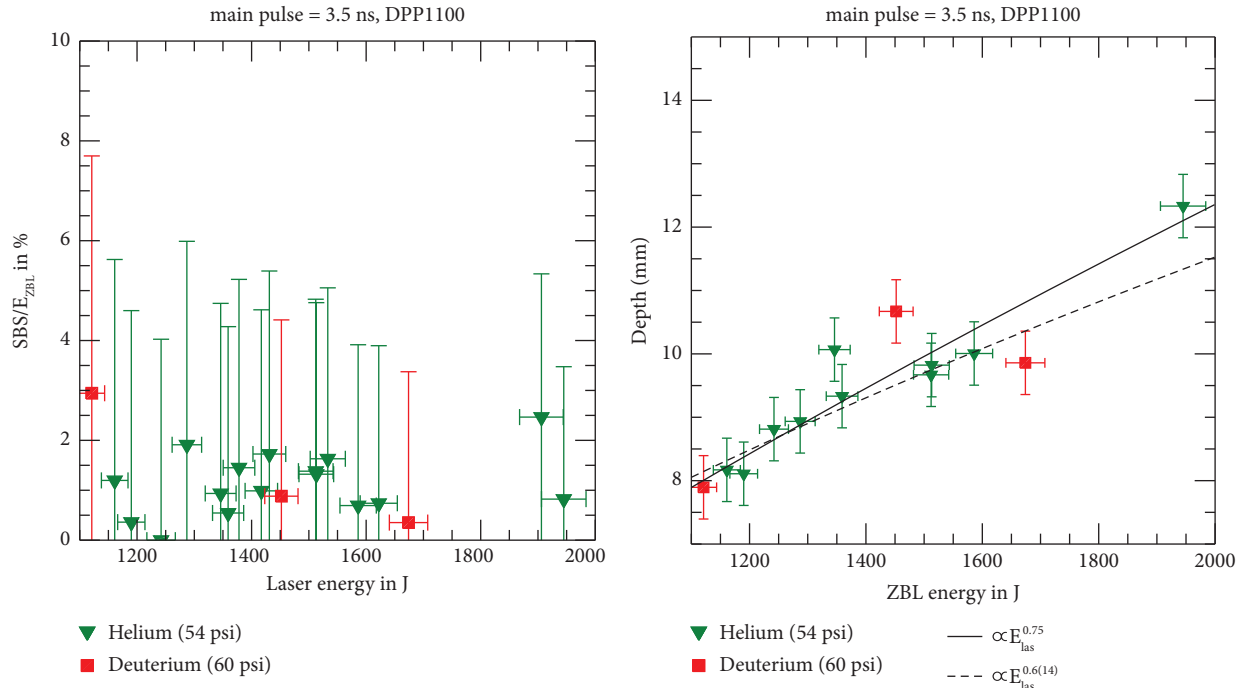
FIGURE 9: Dataset for laser shots with configuration 3 from Table 2.

4. Conclusions

Using helium as a low-hazard substitute for deuterium in laser-heating experiments is a plausible measure, but some caveats exist. Quantitative data for high-LPI regimes will only be accessible with the correct gas type, and the propagation depth can only be matched if the density is modified, which, in turn, will affect moderate-to-high LPI. The findings of this study do not include data for gases such as argon or neopentane, but the underlying physics for the findings will clearly apply in those cases as well.

Data Availability

Data for this study can be accessed upon request by contacting mgeisse@sandia.gov, with the caveat that raw data first need to be officially released by a derivative classifier of Sandia National Laboratories.

Disclosure

This study describes objective technical results and analysis. Any subjective views or opinions that might be expressed in the paper do not necessarily represent the views of the U.S. Department of Energy or the United States Government.

Conflicts of Interest

The authors declare that there are no conflicts of interest.

Acknowledgments

References

[1] D. E. Hinkel, D. A. Callahan, J. D. Moody et al., "Laser-plasma interactions in drive campaign targets on the national ignition facility," *Journal of Physics: Conf. Ser.*, vol. 688, Article ID 012031, 2016.

[2] M. Geissel, A. J. Harvey-Thompson, T. J. Awe et al., "Minimizing scatter-losses during pre-heat for magneto-inertial fusion targets," *Physics of Plasmas*, vol. 25, no. 2, Article ID 022706, 2018.

[3] S. A. Slutz, M. C. Herrmann, R. A. Vesey et al., "Pulsed-power-driven cylindrical liner implosions of laser preheated fuel magnetized with an axial field," *Physics of Plasmas*, vol. 17, no. 5, Article ID 056303, 2010.

[4] S. A. Slutz and R. A. Vesey, "High-gain magnetized inertial fusion," *Physical Review Letters*, vol. 108, no. 2, Article ID 025003, 2012.

[5] A. J. Harvey-Thompson, M. R. Weis, E. C. Harding et al., "Diagnosing and mitigating laser preheat induced mix in MagLIF," *Physics of Plasmas*, vol. 25, no. 11, Article ID 112705, 2018.

[6] C. Labaune, E. Fabre, A. Michard, and F. Briand, "Evidence of stimulated Brillouin backscattering from a plasma at short laser wavelengths," *Physics Reviews*, vol. 32, no. 1, pp. 577–580, 1985.

[7] D. H. Froula, L. Divol, and S. H. Glenzer, "Measurements of nonlinear growth of ion-acoustic waves in two-ion-species plasmas with thomson scattering," *Physical Review Letters*, vol. 88, no. 10, Article ID 105003, 2002.

[8] D. S. Montgomery, "Two decades of progress in understanding and control of laser plasma instabilities in

indirect drive inertial fusion," *Physics of Plasmas*, vol. 23, no. 5, Article ID 055601, 2016.

[9] L. Landau, "On the vibrations of the electronic plasma," *Journal of Physics*, vol. 10, p. 25, 1946.

[10] D. Biskamp and H. Welter, "Stimulated Raman scattering from plasmas irradiated by normally and obliquely incident laser light," *Physical Review Letters*, vol. 34, no. 6, pp. 312–316, 1975.

[11] E. A. Williams, R. L. Berger, R. P. Drake et al., "The frequency and damping of ion acoustic waves in hydrocarbon (CH) and two-ion-species plasmas," *Physics of Plasmas*, vol. 2, no. 1, pp. 129–138, 1995.

[12] S. C. Wilks, W. L. Kruer, J. Denavit et al., "Nonlinear theory and simulations of stimulated Brillouin backscatter in multispecies plasmas," *Physical Review Letters*, vol. 74, no. 25, pp. 5048–5051, 1995.

[13] R. P. Drake, R. E. Turner, B. F. Lasinski et al., "Studies of Raman scattering from overdense targets irradiated by several kilojoules of 0.53 μm laser light," *The Physics of Fluids*, vol. 31, no. 10, pp. 3130–3142, 1988.

[14] S. Atzeni and J. Meyer-Ter-Vehn, *The Physics of Inertial Fusion"*, Oxford University Press, New York, NY, USA, 2004.

[15] P. K. Rambo, I. C. Smith, J. L. Porter Jr. et al., "Z-Beamlet: a multikilojoule, terawatt-class laser system," *Applied Optics*, vol. 44, no. 12, p. 2421, 2005.

[16] R. R. Paguio, G. E. Smith, J. L. Taylor et al., "Evolution of gas cell targets for magnetized liner inertial fusion experiments at the sandia national laboratories PECOS test facility," *Fusion Science and Technology*, vol. 73, no. 3, pp. 414–422, 2018.

[17] Plaskolite LLC, *Plaskolite Product Guide*, Plaskolite LLC, Ohio, OH, USA, 2022.

[18] Wiley, *Optical PTFE the Reference for Light*, Berghof Flouroplastic Technology GmbH, Eningen, Germany, 2014.

[19] A. J. Harvey-Thompson, M. Geissel, C. A. Jennings et al., "Constraining preheat energy deposition in MagLIF experiments with multi-frame shadowgraphy," *Physics of Plasmas*, vol. 26, no. 3, Article ID 032707, 2019.

[20] L. Claus, G. Robertson, L. Fang et al., "Initial characterization results of a 1024x448, 25-um multi-frame camera with 2ns integration time for the Ultrafast X-ray Imager (UXI) program at Sandia National Laboratories," *Proceedings of SPIE*, vol. 9966, pp. 99660F-99661F, 2016.

[21] S. N. Dixit, K. A. Nugent, J. K. Lawson, K. R. Manes, and H. T. Powell, "Kinoform phase plates for focal plane irradiance profile control," *Optics Letters*, vol. 19, no. 6, p. 417, 1994.

[22] Y. Lin, G. N. Lawrence, and T. J. Kessler, "Distributed phase plates for super-Gaussian focal-plane irradiance profiles," *Optics Letters*, vol. 20, no. 7, p. 764, 1995.

[23] D. H. Froula, L. Divol, N. B. Meezan et al., "Ideal laser-beam propagation through high-temperature ignition hohlraum plasmas," *Physical Review Letters*, vol. 98, no. 8, Article ID 085001, 2007.

[24] J. Denavit and D. W. Phillion, "Laser Ionization and heating of gas targets for long-scale-length instability experiments," *Physics of Plasmas*, vol. 1, no. 6, pp. 1971–1984, 1994.